

VALIDITY OF SOUND-PROOF APPROACHES IN RAPIDLY-ROTATING COMPRESSIBLE CONVECTION: MARGINAL STABILITY VS. TURBULENCE

JAN VERHOEVEN* and GARY A. GLATZMAIER

Earth and Planetary Sciences Department, University of California Santa Cruz, CA, USA

(v4.4 released October 2012)

The validity of the anelastic approximation has recently been questioned in the regime of rapidly-rotating compressible convection in low Prandtl number fluids (Calkins *et al.* 2015b). Given the broad usage and the high computational efficiency of sound-proof approaches in this astrophysically relevant regime, this paper clarifies the conditions for a safe application. The potential of the alternative pseudo-incompressible approximation is investigated, which in contrast to the anelastic approximation is shown to never break down for predicting the point of marginal stability. Its accuracy, however, decreases close to the parameters corresponding to the failure of the anelastic approach, which is shown to occur when the sound-crossing time of the domain exceeds the rotation period, i.e. for rotational Mach numbers greater than one. Concerning the supercritical case, which is naturally characterized by smaller rotational Mach numbers, we find that the anelastic approximation does not show unphysical behavior. Growth rates computed with the linearized anelastic equations converge toward the corresponding fully compressible values as the Rayleigh number increases. Likewise, our fully nonlinear turbulent simulations, produced with our fully compressible and anelastic models and carried out in the parameter range in which Calkins *et al.* (2015b) suspect the anelastic approximation to break down, show good agreement.

Keywords: Rotating compressible convection; Anelastic approximation; Pseudo-incompressible; Sound-proof

1. INTRODUCTION

The interiors of stellar and many planetary bodies can be characterized as compressible rapidly-rotating fluids that have small viscous compared to thermal diffusivities, i.e., Prandtl numbers much less than unity. These astrophysical fluid dynamical systems can be modeled with the fully compressible equations that follow from first principles of physics. Their generality comprises a broad range of temporal and spacial scales corresponding to physical phenomena reaching from sound waves over buoyancy induced flows up to atmospheric jets. Accounting for each of these processes, however, implies high computational costs for numerical simulations. In order to more adequately understand the structure and evolution of planetary and astrophysical objects, it is often favorable to channel all available resources into only the relevant physical phenomena, which has motivated the development of reduced forms of the fully compressible equations. For the purpose of modeling planetary and stellar convection, it is believed that dynamically unimportant sound waves can safely be neglected, which, due to the reduced spectrum of time-scales that needs to be resolved, effectively decreases the necessary computational effort.

Several so-called sound-proof approaches retaining the major compressibility effects are in use for modeling these kind of systems. The most widely employed ones are the anelastic

*Corresponding author. Email: jverhoeven@ucsc.edu

approximation (e.g. Batchelor 1953, Ogura and Phillips 1962, Gough 1969, Gilman and Glatzmaier 1981, Braginsky and Roberts 1995, Lantz and Fan 1999, Jones *et al.* 2009, Glatzmaier 2014, Verhoeven *et al.* 2015), the pseudo-incompressible approximation (Durran 1989, 2008, Klein and Pauluis 2012, Vasil *et al.* 2013, Wood and Bushby 2016), and the closely related low Mach number approach (Majda and Sethian 1985, Bell *et al.* 2004, Almgren *et al.* 2006a,b, 2014). Two necessary conditions for all these approaches to be valid are that the Mach number, which is defined as the ratio of the fluid velocity to the local sound speed, is much smaller than unity and that pressure perturbations are small relative to the depth-dependent background pressure. For the pseudo-incompressible and low Mach number approaches this is also sufficient, but for the anelastic approximation all thermodynamic perturbations from a depth-dependent background state must also be small.

Only few studies are available that verify these theoretical predictions quantitatively for thermal convection, with most of them confirming a good agreement between anelastic and fully compressible computations and paying less attention to the pseudo-incompressible approach. Whereas Berkoff *et al.* (2010) addressed linear magneto-convection, Lecoanet *et al.* (2014) investigated differences between thermal conductivity and large-eddy entropy diffusion (Glatzmaier 1984) and additionally considered the pseudo-incompressible case. This was followed by Calkins *et al.* (2015a) verifying the accuracy of the anelastic approximation at the point of marginal stability under the influence of rotation in Prandtl number unity fluids. However, in a follow-up study Calkins *et al.* (2015b) showed that the linear anelastic equations fail to produce physically meaningful results for marginally stable, rapidly-rotating, low Prandtl number systems. Against their theoretical expectations, they report that this breakdown of the anelastic approximation is caused by the temporal derivative of the density perturbation becoming an important component in the continuity equation. Furthermore, they suspect related problems in the astrophysically relevant nonlinear turbulence regime. So far, Verhoeven *et al.* (2015) carried out the only systematic one-to-one comparison for fully compressible and anelastic turbulent convection, which again proved the functionality of the anelastic equations. They, however, did not consider the problematic regime of rapid-rotation and low Prandtl number.

Although there has been no such study that proves the breakdown of the anelastic approximation for the nonlinear case, the findings of Calkins *et al.* (2015b) are alarming, as they implicitly question the validity of works that investigate astrophysical objects by means of the anelastic equations. There are two possible ways to deal with this problem: Firstly, alternative sound-proof approaches must be studied concerning their applicability at the point of marginal stability. Secondly, the possible breakdown of the anelastic approximation in the astrophysically more relevant turbulence regime must be either confirmed or disproved. Here we extend the work of Calkins *et al.* (2015b) on rapidly-rotating, low Prandtl number compressible convection and present a study on the accuracy of the linear pseudo-incompressible equations at the point of marginal stability. This approach is promising as it retains parts of the problematic temporal derivative of the perturbational density term and thus may provide a more accurate alternative to the anelastic approximation. Furthermore, we present the first one-to-one comparison between fully compressible and anelastic numerical simulations of rapidly-rotating convection in the fully nonlinear turbulent regime at low Prandtl number.

The following questions are addressed:

- How do the anelastic and the pseudo-incompressible approaches vary with respect to their accuracy in predicting the point of marginal stability for rapidly-rotating compressible convection in low Prandtl number fluids?
- Can we identify the physical process constraining their accuracy, which causes the problems found by Calkins *et al.* (2015b)?
- Is it safe to apply the anelastic approximation to the astrophysically relevant fully nonlin-

ear turbulent regime of rapidly-rotating compressible convection at low Prandtl number?

The remainder of this paper is organized as follows. In section 2, we start with defining our idealized model and discussing the differences among the anelastic, pseudo-incompressible and fully compressible approaches. Then in section 3 we describe our numerical results concerning the marginal point of stability, supercritical linear convection and the fully nonlinear turbulence regime. Finally, general conclusions are drawn in section 4.

2. MODEL

In this section the fully compressible, pseudo-incompressible and anelastic linear equations are discussed along with the numerical approach to solve them.

2.1. Governing Equations

Linear compressible convection within a Newtonian ideal gas is investigated in a plane layer geometry rotating with angular velocity $\boldsymbol{\Omega} = \Omega \hat{\mathbf{z}}$. The rotation axis is aligned with the unit vector $\hat{\mathbf{z}}$ and antiparallel to the constant gravity $\mathbf{g} = -g\hat{\mathbf{z}}$. The fluid is characterized by constant specific heat capacities at fixed volume and pressure, c_v and c_p . The dynamic viscosity and thermal conductivity,

$$\mu = \rho\nu \quad (1)$$

$$k_t = c_p \rho \kappa, \quad (2)$$

are taken as fixed functions of z and relate to the kinematic quantities ν and κ , which are the viscous diffusivity and the thermal diffusivity, respectively.

The linear approximation to the governing equations for fully compressible convection describing the temporal evolution of density ρ , fluid velocity \mathbf{v} and entropy s within a reference frame rotating at angular velocity $\boldsymbol{\Omega}$ are

$$\partial_t \rho_1 = -\nabla \cdot (\rho_0 \mathbf{v}), \quad (3)$$

$$\rho_0 \partial_t \mathbf{v} = -\nabla (p_0 + p_1) - (\rho_0 + \rho_1) g \hat{\mathbf{z}} + \nabla \cdot \boldsymbol{\Pi} - 2\Omega \rho_0 \hat{\mathbf{z}} \times \mathbf{v}, \quad (4)$$

$$\rho_0 T_0 \partial_t s_1 = -v_z \rho_0 T_0 \partial_z s_0 + \nabla [k_t \nabla (T_0 + T_1)] + S, \quad (5)$$

with t , p and T specifying time, pressure and temperature, and the indices 0 and 1 denoting the z -dependent background state and its time and 3-D space dependent perturbation, respectively. $\Pi_{ij} = \mu (\partial_j v_i + \partial_i v_j - 2/3 (\nabla \cdot \mathbf{v}) \delta_{ij})$ is the viscous stress tensor for a Newtonian fluid and S denotes a heat source or sink. Note that we have neglected centrifugal forces in equations (3-5) that express the conservation of mass, momentum and energy. They can be closed with an equation of state, i.e. the ideal gas law

$$p_0 = (c_p - c_v) \rho_0 T_0, \quad (6)$$

$$\frac{p_1}{p_0} = \frac{\rho_1}{\rho_0} + \frac{T_1}{T_0}, \quad (7)$$

and a thermodynamic expression relating entropy, temperature and pressure,

$$\frac{\partial_z s_0}{c_p} = \frac{\partial_z T_0}{T_0} - \frac{c_p - c_v}{c_p} \frac{\partial_z p_0}{p_0}, \quad (8)$$

$$\frac{s_1}{c_p} = \frac{T_1}{T_0} - \frac{c_p - c_v}{c_p} \frac{p_1}{p_0}. \quad (9)$$

The background state is chosen to satisfy hydrostatic and thermal equilibrium

$$\partial_z p_0 = -\rho_0 g, \tag{10}$$

$$\partial_z (k_t \partial_z T_0) = -S, \tag{11}$$

which results in these background terms dropping out of equations (4) and (5), respectively. Furthermore, the background temperature gradient

$$\partial_z T_0 = - \left(\frac{g}{c_p} + \frac{\Delta T}{d} \right) \tag{12}$$

is assumed constant in z and defined by the sum of the adiabatic temperature gradient $-g/c_p$ and the ratio of superadiabatic temperature drop, ΔT , prescribed by the boundary conditions and the domain depth d . The background state results from solving equations (6), (8), (10) and (12). Therefore, for a constant thermal conductivity, S vanishes; but, for a constant thermal diffusivity, S is negative, i.e., a heat sink.

2.2. Non-Dimensional Equations

The background state can be non-dimensionalized by using the bottom temperature T_r , bottom density ρ_r , bottom pressure $p_r = (c_p - c_v)\rho_r T_r$ and c_p for entropy. The superadiabatic temperature difference ΔT prescribed by the boundary conditions of the system is chosen to be the scale for the temperature perturbations. As temperature, density and entropy perturbations are usually assumed to be closely correlated in low Mach number flows (see e.g. Clayton 1968), the density and entropy perturbations are scaled correspondingly with $\Delta \rho = \rho_r \Delta T / T_r$ and $\Delta s = c_p \Delta T / T_r$. The domain depth d is used as reference length scale. The velocity is non-dimensionalized with a convective free-fall velocity $v_r = \sqrt{\Delta \rho g d / \rho_r}$ and correspondingly time is scaled with the free-fall time $t_r = d / v_r = \sqrt{\rho_r d / (\Delta \rho g)}$. The pressure perturbation scale $\Delta p = \rho_r v_r^2 = \Delta \rho g d$ is inferred from the fact that pressure extracts kinetic energy from the vertical flows to drive horizontal motions. The scales for viscous and thermal diffusivities ν_r and κ_r are defined as their respective values at the bottom boundary of the domain. When applying these scales, the background state results in

$$\hat{T}_0(\hat{z}) = 1 - (D + \epsilon)\hat{z}, \tag{13}$$

$$\hat{\rho}_0(\hat{z}) = [1 - (D + \epsilon)\hat{z}]^n, \tag{14}$$

$$\hat{p}_0(\hat{z}) = [1 - (D + \epsilon)\hat{z}]^{n+1}, \tag{15}$$

$$\hat{\partial}_z \hat{s}_0(\hat{z}) = - \frac{\epsilon}{\hat{T}_0}, \tag{16}$$

and the governing non-dimensional equations read

$$\frac{\epsilon D}{\gamma - 1} \frac{1}{\hat{T}_0} \hat{\partial}_t \hat{p}_1 - \epsilon \hat{\rho}_0 \hat{\partial}_t \hat{s}_1 = -\hat{\nabla} \cdot (\hat{\rho}_0 \hat{\mathbf{v}}), \quad (17)$$

$$\hat{\rho}_0 \hat{\partial}_t \hat{\mathbf{v}} = -\hat{\nabla} \hat{p}_1 - \hat{\rho}_1 \hat{\mathbf{z}} + \sqrt{\frac{Pr}{Ra}} \hat{\nabla} \cdot \hat{\Pi} - \frac{1}{Ek} \sqrt{\frac{Pr}{Ra}} \hat{\rho}_0 \hat{\mathbf{z}} \times \hat{\mathbf{v}}, \quad (18)$$

$$\hat{\rho}_0 \hat{T}_0 \hat{\partial}_t \hat{s}_1 = \hat{\rho}_0 \hat{v}_z + \frac{1}{\sqrt{Pr Ra}} \hat{\nabla} \cdot (\hat{k}_t \hat{\nabla} \hat{T}_1), \quad (19)$$

$$\hat{\rho}_1 = \frac{D}{\gamma - 1} \frac{1}{\hat{T}_0} \hat{p}_1 - \hat{\rho}_0 \hat{s}_1, \quad (20)$$

$$\hat{s}_1 = \frac{\hat{T}_1}{\hat{T}_0} - D \frac{\hat{p}_1}{\hat{p}_0}, \quad (21)$$

with the hat $\hat{\cdot}$ denoting non-dimensional quantities, e.g. $T_0 = T_r \hat{T}_0$.

2.3. Non-Dimensional Parameters

The following non-dimensional parameters emerge. The dissipation number,

$$D = \frac{gd}{c_p T_r}, \quad (22)$$

defines the absolute value of the non-dimensional global adiabatic temperature gradient. With $-(D + \epsilon)$ being the total dimensionless temperature gradient, see (13), the superadiabaticity of the system is given by

$$\epsilon = \frac{\Delta T}{T_r}. \quad (23)$$

The polytropic index

$$n = \frac{\gamma}{\gamma - 1} \frac{D}{D + \epsilon} - 1, \quad (24)$$

with the ratio of specific heats

$$\gamma = \frac{c_p}{c_v} = \frac{5}{3} \quad (25)$$

being chosen to represent a monatomic ideal gas, is an alternative (dependent) parameter for the superadiabaticity ϵ , with a superadiabatic polytropic index satisfying $n < 1.5$. The adiabatic polytropic index for an ideal monatomic ideal gas (with $\epsilon = 0$) consistently results in

$$n_{ad} = \frac{1}{\gamma - 1} = 1.5. \quad (26)$$

The ratio of superadiabatic to adiabatic temperature gradient ϵ/D often given by 1-D solar models¹ follow from the derivatives of equations (13) and (14),

$$\frac{\epsilon}{D} = \frac{n_{ad} - n}{n + 1}. \quad (27)$$

¹Christensen-Dalsgaard *et al.* (1996) for example specify values for ϵ/D of $O(10^{-4})$ in the bulk of the solar convection zone.

Another useful and widely used parameter is the number of density scale heights

$$N_\rho = \ln \left(\frac{\rho_{bot}}{\rho_{top}} \right) = -n \ln [1 - (D + \epsilon)] \quad (28)$$

specifying the system's density contrast ρ_{bot}/ρ_{top} between bottom and top boundary that can be used instead of the Dissipation number D . The Prandtl number,

$$Pr = \frac{\nu_r}{\kappa_r}, \quad (29)$$

is the ratio of momentum to thermal diffusivity. The Rayleigh number,

$$Ra = \frac{gd^3\Delta T}{\kappa_r\nu_r T_r}, \quad (30)$$

controls the vigor of convection with large g , d , and $\epsilon = \Delta T/T_r$ enhancing and large diffusivities ν and κ reducing the convective vigor. More formally Ra is the ratio of the product of the diffusive timescales d^2/κ_r d^2/ν_r to the square of the free-fall timescale t_r^2 . The Ekman number,

$$Ek = \frac{\nu_r}{2\Omega d^2}, \quad (31)$$

is the ratio of the rotation time scale to the viscous diffusion time scale.

Note that all non-dimensional parameters given in this subsection are defined at the bottom boundary and may vary strongly over the whole domain.

2.4. Differences in the Anelastic, Pseudo-Incompressible and Fully Compressible Equations

The density perturbation term in the continuity equation (17) has been expressed in terms of pressure and entropy by using equation (20) in order to illustrate the approximations carried out in the anelastic and pseudo-incompressible equations in the following.

The anelastic approximation neglects the time derivative of density $\epsilon\hat{\partial}_t\hat{\rho}_1 = \epsilon D/(\gamma - 1)/\hat{T}_0\hat{\partial}_t\hat{p}_1 - \epsilon\hat{\rho}_0\hat{\partial}_t\hat{s}_1$ in the continuity equation (17), which is reasonable as long as all perturbations remain small with $\epsilon \ll 1$. The pseudo-incompressible approximation is less restrictive and only neglects the time derivative of the perturbational pressure term. This approach is justified for low Mach number flows but allows for temperature, density and entropy perturbations to be large¹. In order to check for the validity of both sound-proof approaches the relative magnitudes of the terms being neglected in each approximation, i.e. the perturbational density and pressure terms in the continuity equation

$$\rho_{cont} = \left(\frac{|\epsilon\hat{\partial}_t\hat{\rho}_1|}{\max \left[\left| \hat{\partial}_x(\hat{\rho}_0\hat{v}_x) \right|, \left| \hat{\partial}_y(\hat{\rho}_0\hat{v}_y) \right|, \left| \hat{\partial}_z(\hat{\rho}_0\hat{v}_z) \right| \right]} \right)^{top}, \quad (32)$$

$$p_{cont} = \left(\frac{\epsilon D}{\gamma - 1} \frac{1}{\hat{T}_0} \frac{|\hat{\partial}_t\hat{p}_1|}{\max \left[\left| \hat{\partial}_x(\hat{\rho}_0\hat{v}_x) \right|, \left| \hat{\partial}_y(\hat{\rho}_0\hat{v}_y) \right|, \left| \hat{\partial}_z(\hat{\rho}_0\hat{v}_z) \right| \right]} \right)^{top}, \quad (33)$$

will be quantified for various parameters in this paper. We have chosen to focus on the values at the top boundary as the sound speed is the lowest at this location.

¹Note firstly that the prefactor in the perturbational pressure term equals the squared Mach number (see Appendix B) and secondly that $-\rho_0/c_p\partial_t s_1$, which is the dimensional form of the $-\epsilon\hat{\rho}_0\hat{\partial}_t\hat{s}_1$ term in the continuity equation (17), equals the temporal derivative of the pseudo-incompressible density $\partial_t\rho^*$ as first defined in Durran (1989).

For simplicity we will assume $\epsilon \rightarrow 0 \Leftrightarrow n \rightarrow 1.5$ for each anelastic simulation carried out making the ϵ parameter obsolete, which is common practice when applying the anelastic approximation for nonlinear turbulent convection simulations, see e.g. [Gastine et al. \(2014\)](#), [Heimpel et al. \(2015\)](#). Note that this approach does not increase the error of the anelastic approximation ([Lantz and Fan 1999](#)). Concerning the pseudo-incompressible approach, however, the ϵ parameter is required, as it still appears in the continuity equation (17) in the entropy term.

2.5. Numerical Approach for the Linear Stability Problem

In order to solve the linear equations (17-21) numerically, each variable is represented by the typical normal mode ansatz, e.g. $\hat{T}_1 = \hat{T}(z) \exp \left[\hat{r}t + i \left(\hat{\omega}t + \hat{k}_x \hat{x} + \hat{k}_y \hat{y} \right) \right]$. Here, \hat{r} denotes the growth rate, $\hat{\omega}$ is the oscillation frequency and \hat{k}_x and \hat{k}_y are the horizontal wavenumbers with $\hat{k} = \sqrt{\hat{k}_x^2 + \hat{k}_y^2}$ (not to be confused with the thermal conductivity \hat{k}_t). The equations, as they are solved numerically, are given in Appendix E, with the critical frequency $\hat{\omega}_c$ and the critical Rayleigh number Ra_c being eigenvalues that depend on the critical wavenumber \hat{k}_c , which is determined by using a nested intervals scheme for $\hat{r} = 0$. Growth rates \hat{r} can be determined by prescribing the Rayleigh number Ra and the wavenumber \hat{k} . A positive \hat{r} with a non-zero $\hat{\omega}$ means that the onset of convection is a temporal oscillation of all variables with their mean amplitudes increasing exponentially in time, whereas the instability is non-oscillatory for $\hat{\omega} = 0$. As the solutions corresponding to critical modes \hat{k}_c are independent of the individual choice of \hat{k}_x and \hat{k}_y and manifest themselves in two-dimensional convection rolls, we restrict our linear analysis to the $k_y = 0$ modes for simplicity without losing generality, see [Calkins et al. \(2015b\)](#).

The numerical framework is based on a second order accurate Newton-Raphson-Kantorovich (NRK) method for solving eigenvalue problems. While the computational domain is periodic in horizontal direction, stress free, impermeable and fixed temperature (i.e. $\hat{T}_1 = 0$) top and bottom boundaries are applied.

The numerical approaches for solving the nonlinear fully compressible and anelastic equations, which are given in Appendix A, are described in [Verhoeven and Stellmach \(2014\)](#), [Verhoeven et al. \(2015\)](#).

3. RESULTS

In this section results from a suite of anelastic, pseudo-incompressible and fully compressible computations are presented in order to test their accuracy and limitations. All linear computations shown are carried out at fixed Ekman number $Ek = 10^{-6}$ and reside in the rapidly-rotating geostrophic limit at low Rossby number, i.e. the Coriolis forces are mostly balanced by the pressure gradient and therefore the results will be essentially the same for computations with smaller Ekman numbers. This was shown by [Calkins et al. \(2015b\)](#) for the marginal stability cases and will be checked for the supercritical simulations presented in the following. We start with studying the point of marginally stable convection, which is followed by investigating the onset of convection in a supercritical setup and eventually finish with the fully nonlinear turbulence regime.

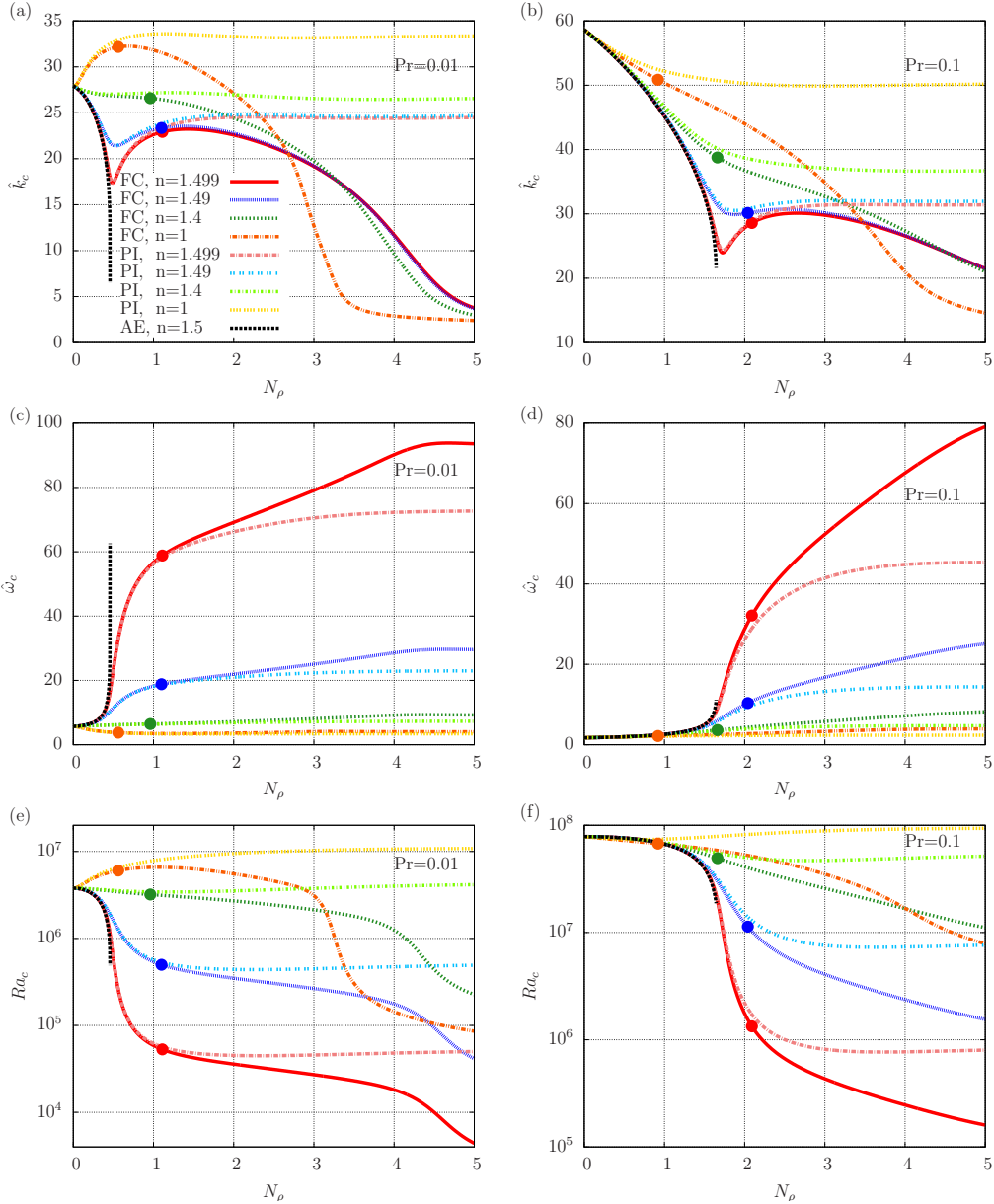


Figure 1. Critical wavenumbers \hat{k}_c (a,b), frequencies $\hat{\omega}_c$ (c,d) and Rayleigh numbers Ra_c (e,f) are plotted against the number of density scale heights N_ρ for different polytropic indices n and $Pr = 0.01$ (a,c,e) and $Pr = 0.1$ (b,d,f). The dynamic viscosity μ and thermal conductivity k_t are constant and the Ekman number $Ek = 10^{-6}$ is fixed for all cases. Results obtained from the pseudo-incompressible equations (PI) are plotted in lighter colors and match the ones provided by the fully compressible equations (FC) in darker colors as long as the relative magnitude of the perturbational pressure term p_{cont} is negligible in the continuity equation, see (33). The transitions to relative magnitudes higher than 0.1 are marked with circles on the fully compressible curves. As shown by [Calkins et al. \(2015b\)](#) the anelastic equations (AE) fail at finite N_ρ (plotted in black). Interestingly, all approaches show the general trend of considerably decreasing critical Rayleigh numbers with decreasing superadiabaticity, i.e. $n \rightarrow 1.5$, at strong density contrasts.

3.1. Marginal Stability

Although linear marginal modes at the onset of convection are not relevant to turbulent convection in stars and planets, we start with the investigation of this topic. This will pave the way for understanding possible problems in sound-proof approaches for supercritical cases. Accordingly, some of the parameter values considered in this subsection do not correspond to an astrophysically achievable system.

Figure 1 shows plots of critical wavenumbers $\hat{k}_c = \sqrt{\hat{k}_x^2 + \hat{k}_y^2}$, frequencies $\hat{\omega}_c$ and Rayleigh

numbers Ra_c against the number of density scale heights $0 \leq N_\rho \leq 5$ for all approaches with various polytropic indices $1 \leq n \leq 1.5$ at low Prandtl numbers $0.01 \leq Pr \leq 0.1$. The results from [Calkins et al. \(2015b\)](#) were reproduced for the anelastic and the fully compressible equations for these constant dynamic viscosity μ and thermal conductivity k_t cases.¹ In contrast to the anelastic approximation that produces infinitely small Ra_c and \hat{k}_c at finite N_ρ , which [Calkins et al. \(2015b\)](#) considered "unphysical", the pseudo-incompressible approach never fails and always produces physically meaningful results with $Ra_c > 0$ and $\hat{k}_c > 0$ in our computations. The results obtained with the pseudo-incompressible equations, however, deviate from those of the fully compressible equations when the relative magnitude of the perturbational pressure term p_{cont} (33) gets larger than $O(0.1)$. These transitions are marked with circles in figure 1 and generally correspond to lower N_ρ the lower the Prandtl number. These results suggest that the anelastic and the pseudo-incompressible approximation both should be applied carefully in marginally stable, rapidly-rotating, low Prandtl number convection systems.

Note that in our simplified model the failure of the anelastic approximation generally involves a drastic decrease in critical wavenumbers k_c corresponding to very large aspect ratios Γ , which are given by the horizontal wavenumber k_c and the depth of the domain d with $\Gamma = 2\pi/(k_c d) = 2\pi/\hat{k}_c$. Instead of solving for Γ , as we do here, one may choose to model marginally stable convection in, for example, a particular spherical shell geometry by prescribing the radii of both the inner and outer boundaries, which sets the value of Γ and so places a lower limit on the possible values of the horizontal wavenumber \hat{k}_c . How this affects the validity of the anelastic approximation for rapidly rotating, low Prandtl number, marginally stable convection is not clear. Two previous studies of this linear stability problem for a 3-D spherical shell [Glatzmaier and Gilman \(1981a,b\)](#), [Drew et al. \(1995\)](#) agree for cases with $Pr = 1$ and 10 but disagree for $Pr = 0.1$. It is worth noting that many anelastic studies of convection in stars and giant planets have modeled the transport of heat by turbulent eddies as a diffusion process based on a turbulent thermal diffusivity and the gradient of entropy, instead of the gradient of temperature. The argument ([Glatzmaier 1984](#)) is that the heat transport by eddies, that are too small to numerically resolve in global models but contribute significantly more heat transport than that by radiation or conduction, should be proportional to the local entropy gradient since turbulence tends to maintain a constant entropy. [Jones et al. \(2009\)](#) has shown that using entropy diffusive heat flux in an anelastic linear stability model of rotating marginally stable convection cannot have negative critical Rayleigh numbers as [Drew et al. \(1995\)](#) found for temperature diffusive heat flux at $Pr = 0.1$.

The constant μ and k_t setup and the corresponding parameter range investigated so far, which has been adopted from [Calkins et al. \(2015b\)](#), involves some problems that might explain the observed breakdown of the anelastic approximation and the inaccuracies in the pseudo-incompressible approach: First, the diffusivities ν and κ vary strongly with height for large N_ρ (see equations 1 and 2) partly resulting in diffusion velocities close to the sound speed. Second, the phase velocity $\hat{v}_{phase} = \hat{\omega}/\hat{k}$, which is the velocity of the pattern of the dominant perturbation corresponding to the oscillatory instability through the domain, exceeds the sound speed for specific parameters. Third, for other parameters the typical rotation time $t_{rot} = 1/(2\Omega)$ falls below the sound-crossing time of the the domain $t_{sound} = d/v_{sound}$. All of these issues potentially introduce timescales shorter than the free-fall time, which hinders the justification of the approximations carried out in sound-proof approaches.

¹Compare figures (1a,b,c,d) to [Calkins et al. \(2015b\)](#) figures (3a,c,b,d), respectively. Note that they plot slightly different values than we do. While they plot $\hat{k}_c Ek^{1/3}$, we plot \hat{k}_c , which effectively makes our values 100 times larger for the $Ek = 10^{-6}$ cases shown. Moreover they scale their critical frequency $\hat{\omega}_c^{Calkins}$ with a timescale inferred from the free-fall velocity based on values at the top boundary, see their equation (2.6). We, however, use reference values at the bottom boundary. The relation between our critical frequency and theirs is given by $\hat{\omega}_c = \exp(N_\rho)^{1/(2n)} \hat{\omega}_c^{Calkins}$. See also their supplementary material for critical Rayleigh numbers.

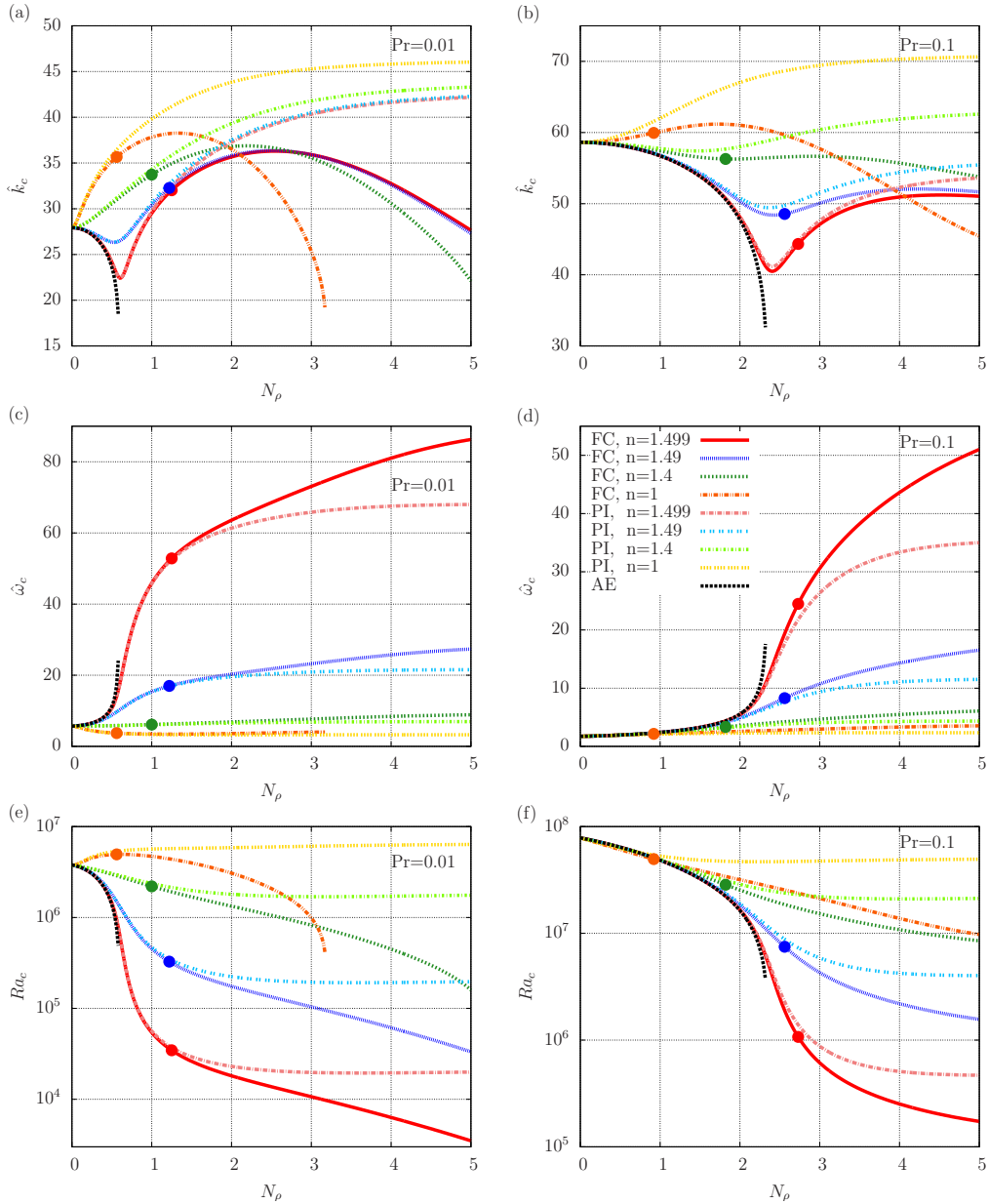


Figure 2. The same as in figure 1, just for constant momentum ν and thermal diffusivities κ rather than constant dynamic viscosity μ and thermal conductivity k_t . The anelastic equations (AE) also fail at finite N_ρ for this case (plotted in black). Interestingly, for $Pr = 0.01$ and $n = 1$ the fully compressible equations become unstable for infinitely small critical wavenumbers \hat{k}_c at $N_\rho \approx 3.2$ (see orange curve in the left panels).

In order to exclude the possibility that the accuracy problems of the anelastic and the pseudo-incompressible approach are an artifact due to the very high diffusivities near the top boundary, figure 2 shows the results from a second series of computations using the same parameters as before but for constant diffusivities ν and κ throughout the domain preventing large diffusion velocities. Although the plots show individual differences to figure 1, the overall result is similar. Alike the anelastic equations that fail to produce physically meaningful outcomes at similar N_ρ as in figure 1, the pseudo-incompressible approach deviates from the fully compressible method at nearby N_ρ compared to the constant μ and k_t case.

Interestingly, our fully compressible computation with constant diffusivities, $Pr = 0.01$ and $n = 1$ yields strongly decreasing critical wavenumbers with $\hat{k}_c \ll 1$ and Rayleigh numbers of $O(10^3)$ as N_ρ approaches a value of approximately 3.2. We speculate that this rather surprising

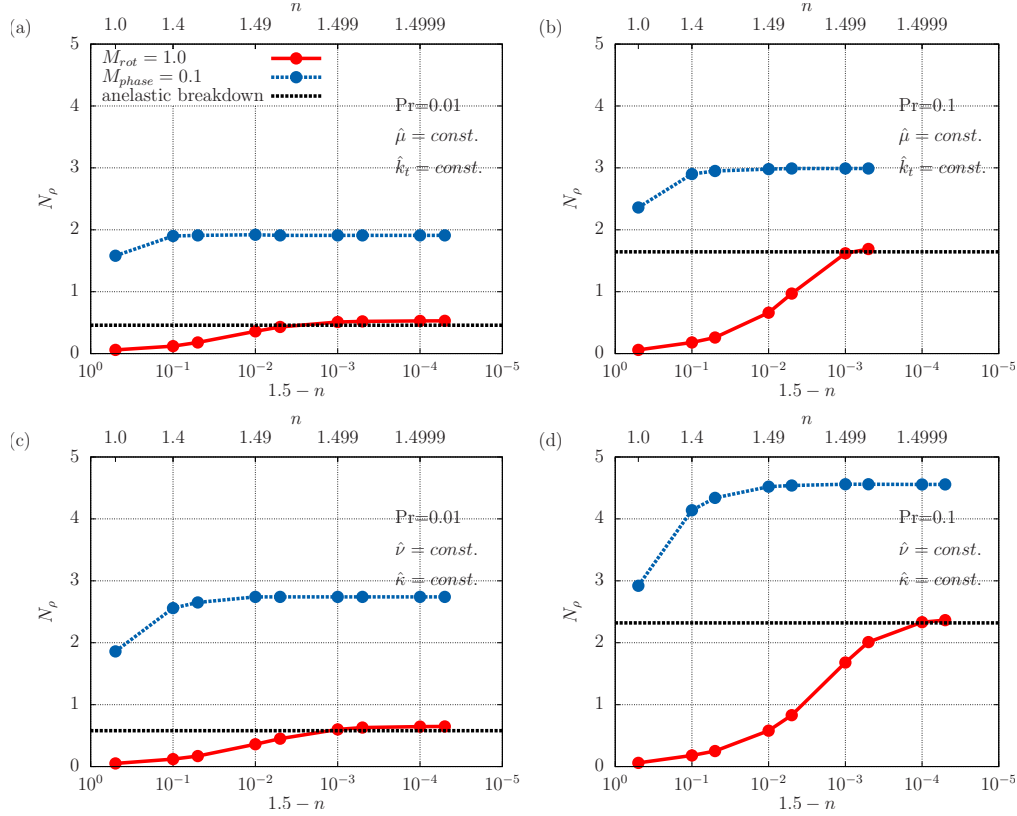


Figure 3. The number of density scale heights N_ρ , for which the rotational Mach number M_{rot} reaches a value of 1 (red) and the phase Mach number M_{phase}^{top} equals 0.1 (blue), is plotted against $n_{ad} - n = 1.5 - n$ for $Ek = 10^{-6}$. It turns out that N_ρ converges against constant values for the anelastic limit $n \rightarrow 1.5$ in all panels representing cases of constant dynamic viscosity and thermal conductivity in the top row (a,b), constant diffusivities at the bottom (c,d), $Pr = 0.01$ on the left (a,c) and $Pr = 0.1$ on the right (b,d). Additionally, the value for N_ρ corresponding to the breakdown of the anelastic approximation is given by the black line, matching the N_ρ representing $M_{rot} = 1$ in the limit $n \rightarrow 1.5$.

result is caused by the influence of the heat sink that is necessary in order to maintain the background state, see equation (11). The investigation of this topic is beyond the scope of this paper and left for future studies.

According to all our results the anelastic and the pseudo-incompressible approximation both seem to lose accuracy when the perturbational density term and the perturbational pressure term, respectively, have magnitudes that cannot be neglected in the continuity equation anymore, see (32-33). In sound-proof approaches it is typically assumed that the magnitude of the neglected perturbational terms relative to the magnitude of the other terms in the continuity equation scale with the square of the Mach number M^2 , with M being defined as the ratio of a typical fluid velocity v_r and the speed of sound $v_{sound} = \sqrt{c_p(c_p - c_v)T/c_v}$, see Appendix B. For linear stability calculations the mean amplitudes of the fluid velocity and thermodynamic perturbations are arbitrary and increase exponentially with time while the background state does not change. Therefore, the regular Mach number M is not a useful diagnostic for linear calculations. However, the phase velocity $\hat{v}_{phase} = \hat{\omega}/\hat{k}$ is independent of time in linear computations. As the sound speed decreases for smaller temperatures, the phase Mach number is the largest at the top boundary where the fluid is cold. Such a phase top Mach number is derived in the non-dimensionalization used here in Appendix C and reads

$$M_{phase}^{top} = M_{phase}^{top} \frac{\hat{\omega}}{\hat{k}} = \sqrt{\frac{\epsilon D}{\gamma - 1}} \exp\left(\frac{N_\rho}{2n}\right) \frac{\hat{\omega}}{\hat{k}}. \quad (34)$$

Additionally, in order for sound-proof approaches to be valid the rotation period must be larger

than the sound-crossing time of the domain (Braginsky and Roberts 1995). A corresponding rotational Mach number can be defined as in appendix D, resulting in

$$M_{rot} = \frac{t_{sound}^{bot}}{t_{rot}} = \frac{2\Omega d}{v_{sound}^{bot}} = \frac{1}{Ek} \sqrt{\frac{\epsilon D Pr}{(\gamma - 1) Ra}}. \quad (35)$$

Please note that for the linear marginal stability case we are considering here, the Rayleigh number in equation (35) must be consistently replaced by Ra_c , which is calculated and not a prescribed parameter as it would be for the supercritical onset of convection or a nonlinear simulation. As both, the phase and the rotational Mach numbers, depend on the superadiabaticity ϵ , no finite values can be determined for our anelastic computations with $\epsilon = 0$ directly. Furthermore, in the anelastic limit, $\epsilon \rightarrow 0$, the critical Rayleigh number can become infinitely small, $Ra_c \rightarrow 0$, prohibiting the calculation of M_{rot} . This can be compensated by using fully compressible computations close to the anelastic limit with $\epsilon \ll 1 \Leftrightarrow 1.5 - n \ll 1$. For $Ek = 10^{-6}$, $Pr = 0.01$ and $Pr = 0.1$, and constant μ and k_t and constant diffusivities ν and κ , figure 3 shows plots of N_ρ , for which the afore mentioned Mach numbers exceed a specific limit, against $1.5 - n$ being proportional to ϵ for $\epsilon \ll 1$. The fully compressible simulations are closest to the anelastic limit for small $1.5 - n$, for which both Mach number cases show convergence against a constant value of N_ρ . Concerning the rotational Mach number case this plateau is caused by the constancy of ϵ/Ra_c in this parameter range; see figure 1. Figure 3 shows that the breakdown of the anelastic approximation (marked by the black line) coincides with the N_ρ corresponding to the rotational Mach number M_{rot} exceeding 1 (red). For comparison the values of N_ρ correlating with the phase Mach number $M_{phase} = 0.1$ are displayed in blue. The limit of 0.1 was chosen, as the limit of 1 was not exceeded for the computations with small $1.5 - n$.

In summary, the accuracy of the anelastic approximation for marginally stable convection is controlled by the rotational Mach number M_{rot} in our simulations. Our results suggest that Calkins *et al.* (2015b) found the anelastic equations to fail, as the typical rotation time was smaller than the sound-crossing time of the domain in their respective simulations. We speculate that the pseudo-incompressible approximation has a more gentle changeover to being imprecise than the anelastic approximation to failure because the temporal derivative term in the continuity equations compensates for the missing pressure term and allows for numerically stable but nevertheless inaccurate solutions.

3.2. Supercritical Onset of Convection

So far, we focussed on the marginal point of stability only. Natural systems, however, are often characterized by strongly supercritical Rayleigh numbers, $Ra \gg Ra_c$, which in combination with small superadiabaticity leads to small rotational Mach numbers, see equation (35). As the supercriticality increases, non-oscillatory (i.e. $\hat{\omega} = 0$) convective instabilities emerge. The critical wavenumbers $\hat{k}_c^{non-osc}$ and Rayleigh numbers $Ra_c^{non-osc}$ corresponding to this kind of instability do not depend on the Prandtl number and are given in figure 4 for the anelastic ($n = 1.5$) and the fully compressible case ($n = 1.49$) with $Ek = 10^{-6}$ and constant μ and k_t . In contrast to the oscillatory instability, both cases closely match for all N_ρ considered.

The relative magnitudes of the time derivative term in the continuity equation at the top boundary ρ_{cont} , see (32), is plotted against the Rayleigh number for oscillatory and non-oscillatory fully compressible linear convection in figure 5 for $n = 1.49$, $Pr = 0.1$ and different Ekman numbers and numbers of density scale heights. The outcome of figure 5 is twofold: First, the results shown do not vary for $Ek \leq O(10^{-6})$ for $N_\rho = 2$ in the left panel, and for $Ek \leq O(10^{-7})$ for $N_\rho = 5$ in the right panel as the geostrophic limit is reached for all corresponding Rayleigh numbers displayed. Second, ρ_{cont} decreases for increasing Ra , with $\rho_{cont} \ll 1$ for

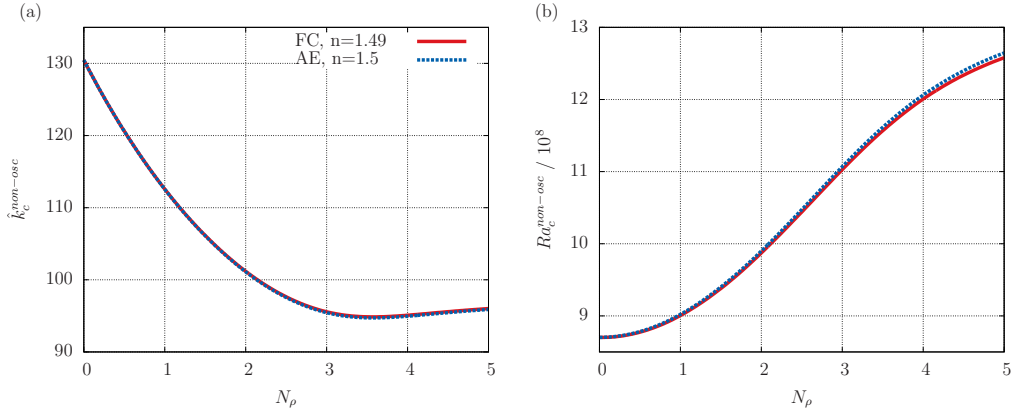


Figure 4. Critical wavenumbers $\hat{k}_c^{non-osc}$ (a) and Rayleigh numbers $Ra_c^{non-osc}$ (b) for non-oscillatory convection are plotted against the number of density scale heights N_ρ for the fully compressible (red) and the anelastic (blue) case. The results from both approaches closely match and are independent of the Prandtl number Pr . The dynamic viscosity μ and thermal conductivity k_t are constant and the Ekman number $Ek = 10^{-6}$ is fixed for both cases.

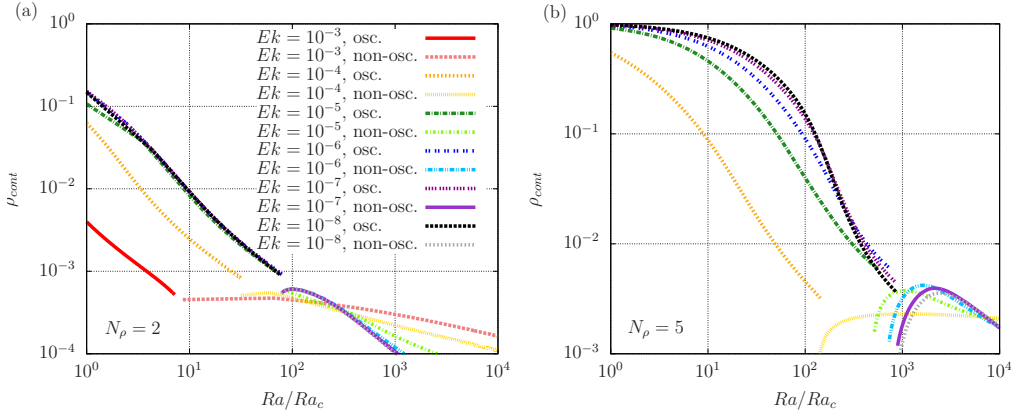


Figure 5. The relative magnitudes of the time derivative term in the continuity equation ρ_{cont} is plotted against the Rayleigh number for oscillatory and non-oscillatory fully compressible linear convection for different Ekman numbers, $n = 1.49$, $Pr = 0.1$ and $N_\rho = 2$ in panel (a) and $N_\rho = 5$ in panel (b). ρ_{cont} strongly depends on the Rayleigh number and is noncontinuous for $Ra = Ra_c^{non-osc}$. The time derivative term is negligible with $\rho_{cont} \ll 1$ for all Rayleigh numbers larger than $Ra_c^{non-osc}$. The asymptotic limit, i.e. geostrophy, is reached for $Ek \leq O(10^{-6})$ for $N_\rho = 2$ and $Ek \leq O(10^{-7})$ for $N_\rho = 5$.

$Ra > Ra_c^{non-osc}$. This strongly suggests the functionality of the anelastic approximation for large Rayleigh numbers for rapidly-rotating convection, although the Prandtl number is low, the density contrast is large and the geostrophic limit is reached.

In order to further ascertain this, the growth rates \hat{r} corresponding to both non-oscillatory and oscillatory instabilities for anelastic and fully compressible convection are displayed in figure 6 for $Ek = 10^{-6}$ and $Pr = 0.1$. For given Rayleigh numbers Ra , numbers of density scale heights N_ρ and polytropic indices n , the growth rates \hat{r} are plotted against the wavenumber \hat{k} . The anelastic approximation neither fails nor gives rise to spurious growth for any parameters investigated in the supercritical regime. In fact fully compressible growth rates generally converge to the anelastic limit case for $n \rightarrow 1.5$. While \hat{r} strongly varies between different polytropic indices for large N_ρ and low Ra , the match increases for lower N_ρ and larger Ra , with the latter seeming to be the most relevant parameter. For moderately high $Ra = 2Ra_c^{non-osc}$ the growth rates of non-oscillatory and oscillatory instabilities are indistinguishable for $n \geq 1.49$ and just differ to the ones for $n = 1.2$ within a few percent.

In summary, the breakdown of the anelastic approximation found by Calkins *et al.* (2015b) is due to a purely linear phenomenon that vanishes for rotational Mach numbers smaller than one, which is fulfilled for large enough Rayleigh numbers. Given the very high Rayleigh

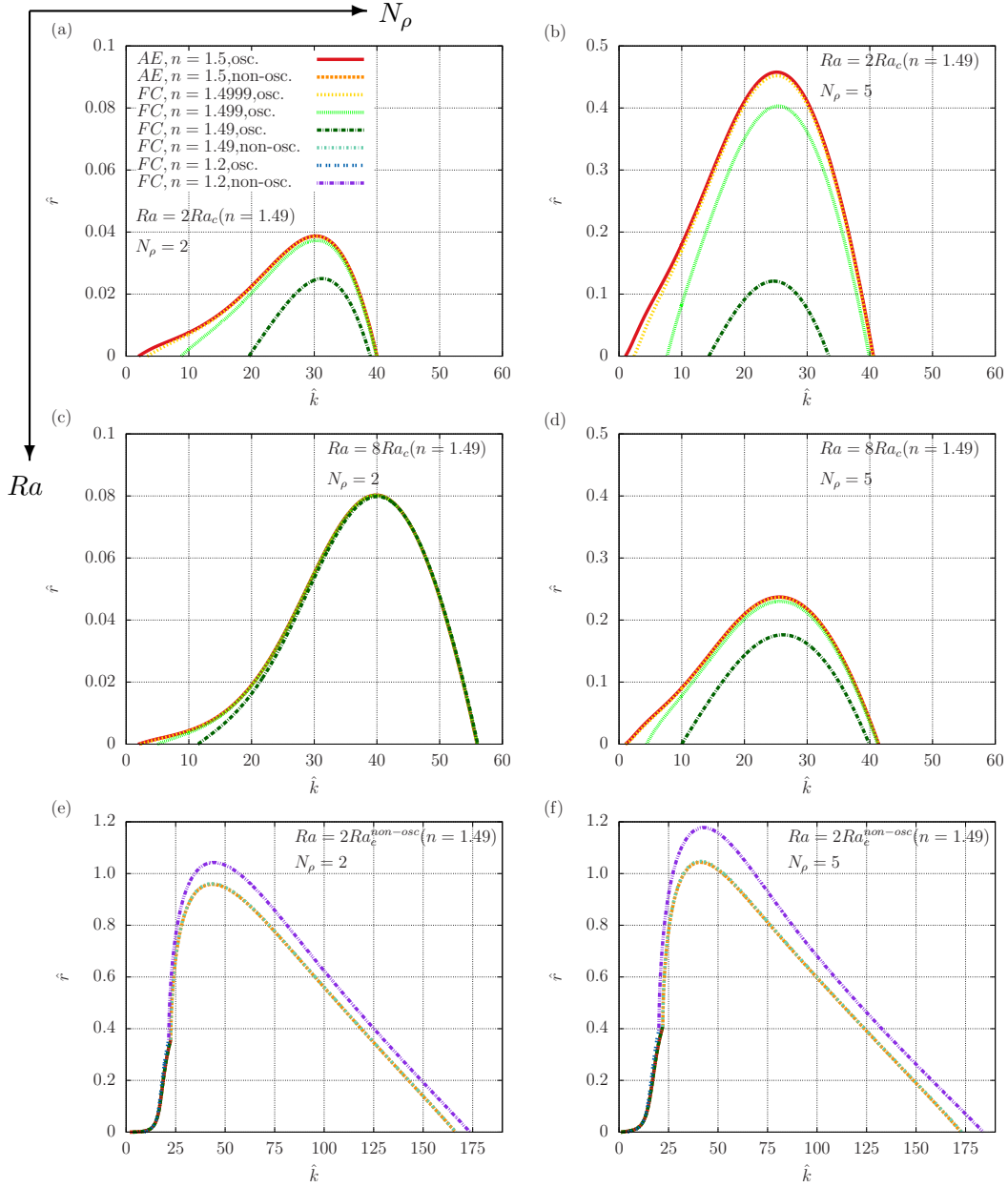


Figure 6. Growth rates $\hat{\tau}$ are plotted against the wavenumber \hat{k} for different Rayleigh numbers Ra , numbers of density scale heights N_ρ and polytropic indices n for $Pr = 0.1$. Rayleigh numbers increase from the top to the bottom panels with $Ra = 2Ra_c(n = 1.49, N_\rho)$ in (a) and (b), $Ra = 8Ra_c(n = 1.49, N_\rho)$ in (c) and (d) and $Ra = 2Ra_c^{non-osc}(n = 1.49, N_\rho)$ in (e) and (f), whereas the number of density scale heights increases from the left to the right panels with $N_\rho = 2$ in (a), (c) and (e) and $N_\rho = 5$ in (b), (d) and (f). The growth rates of the oscillatory instability associated with different polytropic indices are color coded for the anelastic limit $n = 1.5$ in red, for the fully compressible cases $n = 1.4999$ in yellow, $n = 1.499$ in light green, $n = 1.49$ in dark green and $n = 1.2$ in blue. Growth rates of the non-oscillatory instability are plotted in orange for $n = 1.5$, in turquoise for $n = 1.49$ and in purple for $n = 1.2$. While $\hat{\tau}$ strongly varies between different polytropic indices for large N_ρ and low Ra , the match increases for lower N_ρ and larger Ra , with the latter being the most constraining parameter. For the $Ra = 2Ra_c^{non-osc}$ cases shown in panels (e) and (f), the growth rates of both kinds of instabilities are indistinguishable for $n \geq 1.49$ and just differ to the ones for $n = 1.2$ within a few percent..

numbers required for nonlinear turbulent convection, this strongly suggests the insignificance of this phenomenon for the turbulence regime relevant to planets and stars.

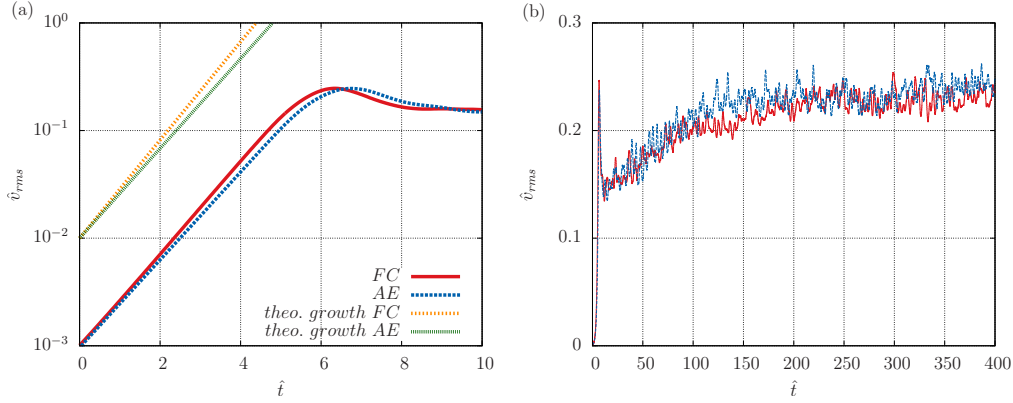


Figure 7. The time evolution of the root-mean-square velocities \hat{v}_{rms} is plotted against time for nonlinear simulations. Panel (a) displays the exponential growth of the convective instability in the nonlinear fully compressible (red) and anelastic (blue) simulations with $Pr = 0.1$, $Ek = 10^{-6}$ and $Ra = 1.98 \times 10^9$, $N_\rho^{ad} = 2$. Both cases match their expected growth rates corresponding to the non-oscillatory instabilities with $\hat{r}_{FC} = 1.05$ (orange) and $\hat{r}_{AE} = 0.96$ (green). Panel (b) shows the long-term evolution of v_{rms} for both cases. After the first five free-fall times characterized by exponential growth, a large-scale cyclonic vortex emerges, which accumulates kinetic energy until about $\hat{t} = 200$ when the simulations reach statistical equilibrium. The time averaged root-mean-square velocities and their standard deviations for $200 \leq \hat{t} \leq 400$ result in $\langle \hat{v}_{rms}^{FC} \rangle = 0.228 \pm 0.009$ and $\langle \hat{v}_{rms}^{AE} \rangle = 0.233 \pm 0.010$, a difference of about 2%.

3.3. Nonlinear Turbulent Convection

In order to test the functionality of the anelastic approximation in rapidly-rotating turbulent convection in low Prandtl number fluids, a one-to-one comparison with constant μ and k_t is carried out in the parameter range where [Calkins et al. \(2015b\)](#) suspect the breakdown of the anelastic equations.

The employed parameters for the fully nonlinear anelastic simulation are $Pr = 0.1$, $Ek = 10^{-6}$, $N_\rho = 2$ and the Rayleigh number is defined by two times the critical value for non-oscillatory anelastic convection given in figure 4, which yields $Ra \approx 1.98 \times 10^9$. The choice of these parameters ensures a major role of Coriolis forces with a convective Rossby number ([Gilman 1977](#)) of $Ro_c = Ek \sqrt{Ra/Pr} \approx 0.14$ and correspond to the geostrophic limit according to the linear results shown in figure (5). For the corresponding fully compressible computation we have to additionally provide the superadiabaticity, which is chosen to be $\epsilon = 0.1$. This choice of the superadiabaticity is a trade-off between a low value, which is predicted for planetary and stellar convection zones, to computational feasibility. We further keep the adiabatic number of density scale heights $N_\rho^{ad} = 2$, which yields $N_\rho \approx 2.17$ and $n \approx 1.20$. The aspect ratio $\Gamma = l_x/d = l_y/d$, i.e. the horizontal width divided by the domain height, is inspired by the critical wavenumber associated with the non-oscillatory instability. The choice of $\Gamma \approx 0.39$ ensures that several wavelengths of the critical non-oscillatory (~ 6) and oscillatory instabilities (~ 2) fit into the domain in each horizontal direction, see figures 1 and 4.

The anelastic and the fully compressible simulations turn out to be very similar. Figure 7 shows the time evolution of the root-mean-square velocity

$$\hat{v}_{rms} = \sqrt{\frac{1}{\hat{V}} \int d\hat{V} \hat{v}^2}, \quad (36)$$

with \hat{V} being the volume of the domain, for the fully compressible and the anelastic simulation in red and blue, respectively. Panel (a) displays the exponential growths of v_{rms} , which match the theoretical predictions for the fully compressible (orange) and anelastic (green) non-oscillatory instabilities. Panel (b) shows the long-time evolution of v_{rms} being qualitatively the same for both cases. After the first five free-fall times characterized by exponential growth, one large-scale cyclonic vortex emerges in each simulation, which accumulates kinetic energy until about $\hat{t} = 200$ when the computations reach statistical equilibrium. The time-

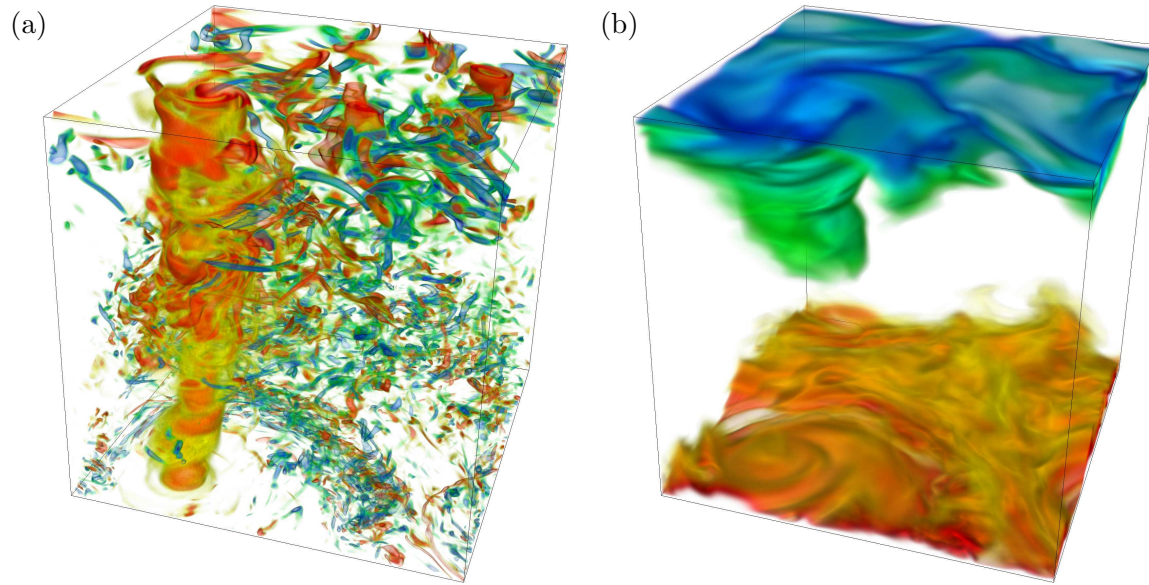


Figure 8. (a) Dynamics in an anelastic simulation run that reached statistical equilibrium, which is illustrated by a volume rendering of the vertical vorticity $\hat{\omega}_z$. While red and yellow colors denote positive $\hat{\omega}_z$, blue and green signify negative $\hat{\omega}_z$. Most conspicuous is the emergence of a large-scale cyclonic vortex, whose angular momentum is balanced by many small-scale anticyclones. (b) The corresponding superadiabatic temperature \hat{T}_1 is displayed with red specifying hot and blue indicating cold material. The employed parameters are $Ra = 1.98 \times 10^9$, $Pr = 0.1$, $Ek = 10^{-6}$ and $N_\rho = 2$, which is in the regime of the suspected breakdown of the anelastic approximation. Nevertheless, corresponding snapshots taken from numerical simulations of fully compressible convection look qualitatively the same and are visually indistinguishable from the example at hand. For better visibility, the domain has been horizontally stretched by a factor of 2.5.

averaged fully compressible value for v_{rms} matches the corresponding anelastic one within 2% in this final state. Also the net heat transport in terms of the Nusselt number

$$Nu = -\partial_z \langle \hat{T}_1 \rangle \Big|_{\hat{z}=0}, \tag{37}$$

where the angle brackets imply temporal and horizontal averaging, turns out to be comparable in the final state, with $Nu = 13.2$ for the anelastic and $Nu = 12.2$ for the fully compressible case representing a difference of roughly 8%. This conformity in the output parameters agrees with direct comparisons of anelastic and fully compressible non-rotating convection (Verhoeven *et al.* 2015) and shows (albeit indirectly) that the time derivative of the density fluctuation in the continuity equation is not important in our nonlinear simulations.

In order to give a visual impression of the fluid dynamics, figure 8 shows snapshots of the anelastic simulation in statistical equilibrium displaying (a) the vertical vorticity

$$\hat{\omega}_z = \hat{\partial}_x \hat{v}_y - \hat{\partial}_y \hat{v}_x \tag{38}$$

and (b) the superadiabatic temperature \hat{T}_1 . Panel (a) clearly shows the large-scale cyclonic vortex (red), whose angular momentum is balanced by many small-scale anticyclones (blue). In panel (b) cold material (blue) is located near the top and hot fluid (red) close to the bottom boundary.

Such symmetry breaking single large-scale cyclonic vortices typically emerge on the verge of the regime of nonlinear rapid rotation, see e.g. Guervilly *et al.* (2014), Favier *et al.* (2014). Ekman numbers of $O(10^{-7})$ and below are necessary in order to reach the nonlinear geostrophic turbulence regime, in which strong cyclonic and anticyclonic vortices are generated with the symmetry being restored (Stellmach *et al.* 2014, Rubio *et al.* 2014). Such parameter ranges are clearly desirable, albeit not accessible with our fully compressible code, which prevents us from carrying out a direct comparison with anelastic results for these extreme parameters. A broader parameter range needs to be tested in future studies.

4. CONCLUSIONS

The validity of the anelastic approximation in the astrophysically relevant regime of rapidly-rotating compressible convection has recently been questioned by [Calkins *et al.* \(2015b\)](#). The high computational efficiency and broad application of sound-proof approaches provided the motivation for this paper, that extended their work by further constraining and reviewing the applicability of different sound-proof models in this regime.

As a starting point we focussed on the pseudo-incompressible approximation ([Durrán 1989](#)), which comprises more discreet simplifications in comparison to the anelastic approach. This is indeed reflected in our computations and in contrast to the anelastic approximation, the pseudo-incompressible approach does not fail in linear stability calculations at the point of marginal stability. Instead its results slowly deviate from the fully compressible solution as the perturbational pressure term in the continuity equation becomes more and more non-negligible, which is usually the case for an increasing number of density scale heights and decreasing Prandtl number shortly after the anelastic approximation breaks down. Our results confirm what [Calkins *et al.* \(2015b\)](#) conclude about anelastic models of marginally stable convection; i.e., that the anelastic approximation for compressible convection in the rapidly-rotating low Prandtl number regime can be inaccurate at marginal stability. We find that the anelastic approach breaks down for simulations, in which the sound-crossing time of the computational domain exceeds the rotation period. Correspondingly, a rotational Mach number is defined as the ratio of both values, which in analogy to the classical Mach number needs to be small in order for sound-proof approaches to be valid.

As the rotational Mach number is inversely proportional the square-root of the Rayleigh number, the situation is much different for higher supercriticality, where the anelastic approximation neither fails nor gives rise to spurious growth for any parameters investigated. Instead our computed fully compressible growth rates generally converge against the ones of the anelastic limit case as the superadiabaticity decreases. In this regime, we found the Rayleigh number to be the most constraining parameter in the sense that low values—close to marginal stability—show distinct differences between anelastic and fully compressible results, whereas moderately high values—of the order of the critical value of non-oscillatory convection—were sufficient to yield a match within a few percent for moderately low superadiabaticities. As Rayleigh numbers in planetary and stellar convection systems are often much higher and superadiabaticities lower than this, we expect the *linear effect* causing the breakdown of the anelastic approximation at marginal stability to be insignificant in such systems and predict the agreement between the approximated and the full equations to get even closer.

These findings could be confirmed by fully nonlinear turbulent convection simulations. The computations in the regime where [Calkins *et al.* \(2015b\)](#) suspected the breakdown of the anelastic approximations, showed close qualitative and quantitative agreement between the anelastic and the fully compressible case. However, further work needs to be done in order to exclude effects other than the one suggested by [Calkins *et al.* \(2015b\)](#), which may cause problems in the anelastic approximation in the geostrophic turbulence regime.

To sum up, the anelastic approximation breaks down for rapidly-rotating compressible convection in low Prandtl number fluids at the point of marginal stability when the rotational Mach number is greater than one. According to our results, however, these problems disappear in the astrophysically more relevant regime of turbulence typically characterized by small rotational Mach numbers. Although we did not specifically test the pseudo-incompressible approximation for supercritical convection, we do not see any reason why the same should not be true for this less invasive approach.

Acknowledgments

We would like to thank two anonymous reviewers for comments that greatly improved the manuscript. We gratefully acknowledge that Prof. Pascale Garaud from UCSC provided her NRK routines, which were the basis of our linear convection code. Support was provided for J.V. by the National Aeronautics and Space Administration under grants OPR NNX13AK94G and PGG NNX14AN70G. The simulations were run at UCSC on the Hyades supercomputer obtained with an MRI grant from the National Science Foundation.

References

- Almgren, A. S., Bell, J. B., Rendleman, C. A., and Zingale, M. (2006a). Low Mach number modeling of type Ia supernovae. I. Hydrodynamics. *The Astrophysical Journal*, **637**(2), 922–936.
- Almgren, A. S., Bell, J. B., Rendleman, C. A., and Zingale, M. (2006b). Low Mach number modeling of type Ia supernovae. II. Energy evolution. *The Astrophysical Journal*, **649**(2), 927–938.
- Almgren, A. S., Bell, J. B., Nonaka, A., and Zingale, M. (2014). Low Mach number modeling of stratified flows. In *Finite Volumes for Complex Applications VII-Methods and Theoretical Aspects*, pages 3–15. Springer.
- Batchelor, G. (1953). The conditions for dynamical similarity of motions of a frictionless perfect-gas atmosphere. *Quarterly Journal of the Royal Meteorological Society*, **79**(340), 224–235.
- Bell, J. B., Day, M. S., Rendleman, C. A., Woosley, S. E., and Zingale, M. A. (2004). Adaptive low Mach number simulations of nuclear flame microphysics. *Journal of Computational Physics*, **195**(2), 677–694.
- Berkoff, N., Kersalé, E., and Tobias, S. (2010). Comparison of the anelastic approximation with fully compressible equations for linear magnetoconvection and magnetic buoyancy. *Geophysical and Astrophysical Fluid Dynamics*, **104**(5-6), 545–563.
- Braginsky, S. and Roberts, P. (1995). Equations governing convection in Earth’s core and the geodynamo. *Geophysical & Astrophysical Fluid Dynamics*, **79**(1), 1–97.
- Calkins, M. A., Julien, K., and Marti, P. (2015a). Onset of rotating and non-rotating convection in compressible and anelastic ideal gases. *Geophysical & Astrophysical Fluid Dynamics*, **109**(4), 422–449.
- Calkins, M. A., Julien, K., and Marti, P. (2015b). The breakdown of the anelastic approximation in rotating compressible convection: Implications for astrophysical systems. In *Proc. R. Soc. A*, volume 471, page 20140689. The Royal Society.
- Christensen-Dalsgaard, J., Däppen, W., Ajukov, S. V., Anderson, E. R., Antia, H. M., Basu, S., Baturin, V. A., Berthomieu, G., Chaboyer, B., Chitre, S. M., et al. (1996). The current state of solar modeling. *Science*, **272**(5266), 1286–1292.
- Clayton, D. D. (1968). *Principles of stellar evolution and nucleosynthesis*. University of Chicago press.
- Drew, S., Jones, C., and Zhang, K. (1995). Onset of convection in a rapidly rotating compressible fluid spherical shell. *Geophysical & Astrophysical Fluid Dynamics*, **80**(3-4), 241–254.
- Durran, D. R. (1989). Improving the anelastic approximation. *Journal of the Atmospheric Sciences*, **46**(11), 1453–1461.
- Durran, D. R. (2008). A physically motivated approach for filtering acoustic waves from the equations governing compressible stratified flow. *Journal of Fluid Mechanics*, **601**, 365–379.
- Favier, B., Silvers, L., and Proctor, M. (2014). Inverse cascade and symmetry breaking in rapidly rotating boussinesq convection. *Physics of Fluids*, **26**(9), 096605.
- Gastine, T., Heimpel, M., and Wicht, J. (2014). Zonal flow scaling in rapidly-rotating compressible convection. *Physics of the Earth and Planetary Interiors*, **232**, 36–50.
- Gilman, P. A. (1977). Non-linear dynamics of Boussinesq convection in a deep rotating spherical shell. *Geophys. Astrophys. Fluid Dyn.*, **8**, 93–135.
- Gilman, P. A. and Glatzmaier, G. A. (1981). Compressible convection in a rotating spherical shell I. Anelastic equations. *The Astrophysical Journal Supplement Series*, **45**, 335–349.
- Glatzmaier, G. A. (1984). Numerical simulations of stellar convective dynamos. I. The model and method. *Journal of Computational Physics*, **55**(3), 461–484.
- Glatzmaier, G. A. (2014). *Introduction to modeling convection in planets and stars. Magnetic field, density stratification, rotation*. Princeton Series in Astrophysics. Princeton University Press.
- Glatzmaier, G. A. and Gilman, P. A. (1981a). Compressible convection in a rotating spherical shell II. A linear anelastic model. *The Astrophysical Journal Supplement Series*, **45**, 351–380.
- Glatzmaier, G. A. and Gilman, P. A. (1981b). Compressible convection in a rotating spherical shell IV. Effects of viscosity, conductivity, boundary conditions, and zone depth. *The Astrophysical Journal Supplement Series*, **47**, 103–115.
- Gough, D. O. (1969). The anelastic approximation for thermal convection. *Journal of the Atmospheric Sciences*, **26**, 448–456.
- Guervilly, C., Hughes, D. W., and Jones, C. A. (2014). Large-scale vortices in rapidly rotating rayleigh–bénard convection. *Journal of Fluid Mechanics*, **758**, 407–435.

- Heimpel, M., Gastine, T., and Wicht, J. (2015). Simulation of deep-seated zonal jets and shallow vortices in gas giant atmospheres. *Nature Geoscience*, **9**, 19–24.
- Jones, C., Kuzanyan, K., and Mitchell, R. (2009). Linear theory of compressible convection in rapidly rotating spherical shells, using the anelastic approximation. *Journal of Fluid Mechanics*, **634**, 291–319.
- Klein, R. and Pauluis, O. (2012). Thermodynamic consistency of a pseudoincompressible approximation for general equations of state. *Journal of the Atmospheric Sciences*, **69**(3), 961–968.
- Lantz, S. and Fan, Y. (1999). Anelastic magnetohydrodynamic equations for modeling solar and stellar convection zones. *The Astrophysical Journal Supplement Series*, **121**(1), 247–264.
- Lecoanet, D., Brown, B. P., Zweibel, E. G., Burns, K. J., Oishi, J. S., and Vasil, G. M. (2014). Conduction in low Mach number flows. I. Linear and weakly nonlinear regimes. *The Astrophysical Journal*, **797**(2), 94.
- Majda, A. and Sethian, J. (1985). The derivation and numerical solution of the equations for zero Mach number combustion. *Combustion Science and Technology*, **42**(3-4), 185–205.
- Ogura, Y. and Phillips, N. (1962). Scale analysis of deep and shallow convection in the atmosphere. *Journal of the Atmospheric Sciences*, **19**(2), 173–179.
- Rubio, A. M., Julien, K., Knobloch, E., and Weiss, J. B. (2014). Upscale energy transfer in three-dimensional rapidly rotating turbulent convection. *Physical review letters*, **112**(14), 144501.
- Stellmach, S., Lischper, M., Julien, K., Vasil, G., Cheng, J., Ribeiro, A., King, E., and Aurnou, J. (2014). Approaching the asymptotic regime of rapidly rotating convection: Boundary layers versus interior dynamics. *Physical Review Letters*, **113**(25), 254501.
- Vasil, G. M., Lecoanet, D., Brown, B. P., Wood, T. S., and Zweibel, E. G. (2013). Energy conservation and gravity waves in sound-proof treatments of stellar interiors. II. Lagrangian constrained analysis. *The Astrophysical Journal*, **773**(2), 169.
- Verhoeven, J. and Stellmach, S. (2014). The compressional beta effect: A source of zonal winds in planets? *Icarus*, **237**, 143–158.
- Verhoeven, J., Wiesehöfer, T., and Stellmach, S. (2015). Anelastic versus fully compressible turbulent Rayleigh-Bénard convection. *The Astrophysical Journal*, **805**(1), 62.
- Wood, T. S. and Bushby, P. J. (2016). Oscillatory convection and limitations of the Boussinesq approximation. *Journal of Fluid Mechanics*, **803**, 502–515.

Appendix A: NONLINEAR EQUATIONS OF COMPRESSIBLE CONVECTION

Nonlinear equations for fully compressible and anelastic convection for the constant μ and k_t case as given by Verhoeven *et al.* (2015) with additionally considering rotation are displayed below. The background profiles $\hat{\rho}_0$, \hat{T}_0 and \hat{p}_0 are assumed to be adiabatic.

A.1. Fully Compressible Equations

The non-dimensional fully compressible equations read

$$\epsilon \hat{\partial}_t \hat{\rho}_1 + \hat{\nabla} \cdot [(\hat{\rho}_0 + \epsilon \hat{\rho}_1) \hat{\mathbf{v}}] = 0, \quad (\text{A.1})$$

$$\begin{aligned} (\hat{\rho}_0 + \epsilon \hat{\rho}_1) \left[\hat{\partial}_t \hat{\mathbf{v}} + (\hat{\mathbf{v}} \cdot \hat{\nabla}) \hat{\mathbf{v}} \right] &= -\hat{\nabla} \hat{p}_1 - \hat{\rho}_1 \hat{\mathbf{z}} + \sqrt{\frac{Pr}{Ra}} \left[\hat{\nabla}^2 \hat{\mathbf{v}} + \frac{1}{3} \hat{\nabla} (\hat{\nabla} \cdot \hat{\mathbf{v}}) \right] \\ &\quad - \frac{1}{Ek} \sqrt{\frac{Pr}{Ra}} (\hat{\rho}_0 + \epsilon \hat{\rho}_1) \hat{\mathbf{z}} \times \hat{\mathbf{v}}, \end{aligned} \quad (\text{A.2})$$

$$\begin{aligned} (\hat{\rho}_0 + \epsilon \hat{\rho}_1) \left[\hat{\partial}_t \hat{T}_1 + (\hat{\mathbf{v}} \cdot \hat{\nabla}) \hat{T}_1 \right] - D \hat{\rho}_1 \hat{v}_z - D \left[\hat{\partial}_t \hat{p}_1 + (\hat{\mathbf{v}} \cdot \hat{\nabla}) \hat{p}_1 \right] &= \frac{1}{\sqrt{RaPr}} \hat{\nabla}^2 \hat{T}_1 \\ &\quad + 2D \sqrt{\frac{Pr}{Ra}} \left[\hat{e}_{ij} - \frac{1}{3} (\hat{\nabla} \cdot \hat{\mathbf{v}}) \delta_{ij} \right]^2, \end{aligned} \quad (\text{A.3})$$

$$\frac{D}{1 - \frac{1}{\gamma}} \frac{\hat{p}_1}{\hat{p}_0} = \frac{\hat{T}_1}{\hat{T}_0} + \frac{\hat{\rho}_1}{\hat{\rho}_0} + \epsilon \frac{\hat{\rho}_1}{\hat{\rho}_0} \frac{\hat{T}_1}{\hat{T}_0}, \quad (\text{A.4})$$

with $\hat{e}_{ij} = \frac{1}{2} \left(\hat{\partial}_j \hat{v}_i + \hat{\partial}_i \hat{v}_j \right)$ being the strain rate tensor.

A.2. Anelastic Equations

The non-dimensional anelastic equations result from (A.1-A.4) in the limit of $\epsilon \rightarrow 0$,

$$\hat{\nabla} \cdot (\hat{\rho}_0 \hat{\mathbf{v}}) = 0, \quad (\text{A.5})$$

$$\hat{\rho}_0 \left[\hat{\partial}_t \hat{\mathbf{v}} + (\hat{\mathbf{v}} \cdot \hat{\nabla}) \hat{\mathbf{v}} \right] = -\hat{\nabla} \hat{p}_1 - \hat{\rho}_1 \hat{\mathbf{z}} + \sqrt{\frac{Pr}{Ra}} \left[\hat{\nabla}^2 \hat{\mathbf{v}} + \frac{1}{3} \hat{\nabla} (\hat{\nabla} \cdot \hat{\mathbf{v}}) \right] - \frac{1}{Ek} \sqrt{\frac{Pr}{Ra}} \hat{\rho}_0 \hat{\mathbf{z}} \times \hat{\mathbf{v}}, \quad (\text{A.6})$$

$$\begin{aligned} \hat{\rho}_0 \left[\hat{\partial}_t \hat{T}_1 + (\hat{\mathbf{v}} \cdot \hat{\nabla}) \hat{T}_1 \right] - D \hat{\rho}_1 \hat{v}_z - D \left[\hat{\partial}_t \hat{p}_1 + (\hat{\mathbf{v}} \cdot \hat{\nabla}) \hat{p}_1 \right] &= \frac{1}{\sqrt{RaPr}} \hat{\nabla}^2 \hat{T}_1 \\ &+ 2D \sqrt{\frac{Pr}{Ra}} \left[\hat{e}_{ij} - \frac{1}{3} (\hat{\nabla} \cdot \hat{\mathbf{v}}) \delta_{ij} \right]^2, \end{aligned} \quad (\text{A.7})$$

$$\frac{D}{1 - \frac{1}{\gamma} \hat{\rho}_0} \hat{p}_1 = \frac{\hat{T}_1}{\hat{T}_0} + \frac{\hat{\rho}_1}{\hat{\rho}_0}. \quad (\text{A.8})$$

Appendix B: MACH NUMBER

The Mach number M is defined as the ratio of a reference velocity, which we assume to be the free-fall velocity,

$$v_r = \sqrt{\frac{gd\Delta\rho}{\rho_r}} \quad (\text{B.1})$$

to the sound speed

$$\begin{aligned} v_{sound} &= \sqrt{\frac{c_p(c_p - c_v)T}{c_v}} \\ &= \sqrt{\frac{c_p(c_p - c_v)T_r}{c_v}} \hat{\rho}_0^{1/(2n)}, \end{aligned} \quad (\text{B.2})$$

resulting in

$$\begin{aligned} M &= \frac{v_r}{v_{sound}} \\ &= \sqrt{\frac{c_v gd\Delta\rho}{c_p(c_p - c_v)T_r \rho_r}} \hat{\rho}_0^{-1/(2n)} \\ &= \sqrt{\frac{\epsilon D}{\gamma - 1}} \hat{\rho}_0^{-1/(2n)}. \end{aligned} \quad (\text{B.3})$$

Exploiting $\hat{\rho}_0^{top} = \exp(-N_\rho)$ yields the Mach number at the top boundary,

$$M^{top} = \sqrt{\frac{\epsilon D}{\gamma - 1}} \exp\left(\frac{N_\rho}{2n}\right), \quad (\text{B.4})$$

where the sound speed is the lowest and thus M has a maximum.

Appendix C: PHASE MACH NUMBER

The phase Mach number M_{phase} will be defined as the ratio of the phase velocity corresponding to the oscillatory instability

$$\begin{aligned} v_{phase} &= \frac{\omega}{k} \\ &= \sqrt{\frac{gd\Delta T}{T_r}} \frac{\hat{\omega}}{\hat{k}}, \end{aligned} \quad (C.1)$$

to the sound speed

$$\begin{aligned} v_{sound} &= \sqrt{\frac{c_p(c_p - c_v)T}{c_v}} \\ &= \sqrt{\frac{c_p(c_p - c_v)T_r}{c_v}} \hat{\rho}_0^{1/(2n)}, \end{aligned} \quad (C.2)$$

resulting in

$$\begin{aligned} M_{phase} &= \frac{v_{phase}}{v_{sound}} \\ &= \sqrt{\frac{c_v gd\Delta T}{c_p(c_p - c_v)T_r^2}} \frac{\hat{\omega}}{\hat{k}} \hat{\rho}_0^{-1/(2n)} \\ &= \sqrt{\frac{gd}{c_p T_r}} \sqrt{\frac{c_v}{c_p - c_v}} \sqrt{\frac{\Delta T}{T_r}} \frac{\hat{\omega}}{\hat{k}} \hat{\rho}_0^{-1/(2n)} \\ &= \sqrt{\frac{\epsilon D}{\gamma - 1}} \frac{\hat{\omega}}{\hat{k}} \hat{\rho}_0^{-1/(2n)}. \end{aligned}$$

Exploiting $\hat{\rho}_0^{top} = \exp(-N_\rho)$ and equation (B.4) yields the phase Mach number at the top boundary,

$$\begin{aligned} M_{phase}^{top} &= \sqrt{\frac{\epsilon D}{\gamma - 1}} \frac{\hat{\omega}}{\hat{k}} \exp\left(\frac{N_\rho}{2n}\right) \\ &= M_{phase}^{top} \frac{\hat{\omega}}{\hat{k}}, \end{aligned} \quad (C.3)$$

where the sound speed is the lowest and thus M_{phase} has a maximum.

Appendix D: ROTATIONAL MACH NUMBER

The rotational Mach number M_{rot} will be defined as the ratio of the velocity corresponding to the domain depth d and the angular frequency Ω

$$v_{rot} = 2\Omega d, \quad (D.1)$$

to the sound speed at the bottom

$$v_{sound}^{bot} = \sqrt{\frac{c_p(c_p - c_v)T_r}{c_v}}, \quad (D.2)$$

resulting in

$$\begin{aligned}
 M_{rot} &= \frac{v_{rot}}{v_{sound}^{bot}} \\
 &= \sqrt{\frac{4c_v\Omega^2 d^2}{c_p(c_p - c_v)T_r}} \\
 &= \frac{1}{Ek} \sqrt{\frac{\epsilon D Pr}{(\gamma - 1)Ra}}.
 \end{aligned} \tag{D.3}$$

This is equivalent to defining the rotational Mach number as the ratio of the sound-crossing time of the domain to the rotation time,

$$\begin{aligned}
 M_{rot} &= \frac{t_{sound}^{bot}}{t_{rot}} \\
 &= \frac{2\Omega d}{v_{sound}^{bot}},
 \end{aligned} \tag{D.4}$$

based on the sound speed v_{sound}^{bot} at the bottom boundary. Note that the value of t_{sound}^{bot} is similar to the one of the real sound-crossing time $t_{sound} = \int_0^d dz/v_{sound}$.

Appendix E: NUMERICALLY SOLVED LINEAR EQUATIONS

This section summarizes the equations as they are solved in the linear convection code. As it only deals with non-dimensional quantities, the hat $\hat{\cdot}$ is left out for clarity. Equations (17-21) can be simplified by expressing ρ_1 and s_1 in terms of T_1 and p_1 , which reduces the number of equations from five to three,

$$\alpha \frac{\epsilon D}{\gamma - 1} \frac{1}{T_0} \partial_t p_1 + \beta \left(\epsilon D \frac{\rho_0}{p_0} \partial_t p_1 - \epsilon \frac{\rho_0}{T_0} \partial_t T_1 \right) = -\nabla \cdot (\rho_0 \mathbf{v}), \tag{E.1}$$

$$\rho_0 \partial_t \mathbf{v} = -\nabla p_1 + \left(\frac{\rho_0}{T_0} T_1 - \frac{\gamma}{\gamma - 1} D \frac{\rho_0}{p_0} p_1 \right) \mathbf{z} + \sqrt{\frac{Pr}{Ra}} \nabla \cdot \mathbf{\Pi} - \frac{1}{Ek} \sqrt{\frac{Pr}{Ra}} \rho_0 \mathbf{z} \times \mathbf{v}, \tag{E.2}$$

$$\rho_0 \partial_t T_1 - D \partial_t p_1 = \rho_0 v_z + \frac{1}{\sqrt{Pr Ra}} \nabla (k_t \nabla T_1). \tag{E.3}$$

The parameters α and β have been introduced in order to account for the three different approaches under investigation. While in the anelastic approximation the perturbational density term is neglected in the continuity equation (i.e. $\alpha = \beta = 0$), the pseudo-incompressible approximation just neglects the perturbational pressure term resulting in $\alpha = 0$ and $\beta = 1$. The fully compressible equations do not contain any simplifications, thus $\alpha = \beta = 1$. We further define $P_1 = \sqrt{Ra/Pr} p_1$ in order to simplify the numerical method, compare equation (E.2) with (E.11), (E.20).

For the constant dynamic viscosity μ and thermal conductivity k_t case we assume

$$\begin{aligned}
 \mu(z) &= 1 \\
 \mu'(z) &= 0 \\
 k_t(z) &= 1 \\
 k_t'(z) &= 0,
 \end{aligned} \tag{E.4}$$

whereas for constant diffusivities ν and κ the corresponding dynamic viscosity and thermal conductivity vary with depth (see equations 1, 2 and 14),

$$\begin{aligned}\mu(z) &= T_0^n(z) \\ \mu'(z) &= -(D + \epsilon) n T_0^{n-1}(z) \\ k_t(z) &= T_0^n(z) \\ k_t'(z) &= -(D + \epsilon) n T_0^{n-1}(z).\end{aligned}\tag{E.5}$$

Note that the $'$ sign denotes the first derivative in z-direction, i.e. $' = \partial_z$.

When using the typical normal mode ansatz, e.g. $T_1 = T(z) \exp[rt + i(\omega t + k_x x + k_y y)]$, with the wavenumber k_x and k_y not to be confused with the thermal conductivity k_t , equations (E.1-E.3) can be solved separately for the real part (index re),

$$\partial_z v_{x,re} = v'_{x,re} \tag{E.6}$$

$$\begin{aligned}\mu \partial_z v'_{x,re} &= \sqrt{\frac{Ra}{Pr}} r T_0^n v_{x,re} - \sqrt{\frac{Ra}{Pr}} \omega T_0^n v_{x,im} - k_x P_{im} + \mu \left(\frac{4}{3} k_x^2 + k_y^2 \right) v_{x,re} \\ &\quad + \frac{1}{3} \mu k_x k_y v_{y,re} + \frac{1}{3} \mu k_x v'_{z,im} - \mu' v'_{x,re} + \mu' k_x v_{z,im} - \frac{1}{Ek} T_0^n v_{y,re}\end{aligned}\tag{E.7}$$

$$\partial_z v_{y,re} = v'_{y,re} \tag{E.8}$$

$$\begin{aligned}\mu \partial_z v'_{y,re} &= \sqrt{\frac{Ra}{Pr}} r T_0^n v_{y,re} - \sqrt{\frac{Ra}{Pr}} \omega T_0^n v_{y,im} - k_y P_{im} + \mu \left(k_x^2 + \frac{4}{3} k_y^2 \right) v_{y,re} \\ &\quad + \frac{1}{3} \mu k_x k_y v_{x,re} + \frac{1}{3} \mu k_y v'_{z,im} - \mu' v'_{y,re} + \mu' k_y v_{z,im} + \frac{1}{Ek} T_0^n v_{x,re}\end{aligned}\tag{E.9}$$

$$\partial_z v_{z,re} = v'_{z,re} \tag{E.10}$$

$$\begin{aligned}\frac{4}{3} \mu \partial_z v'_{z,re} - \partial_z P_{re} &= \sqrt{\frac{Ra}{Pr}} r T_0^n v_{z,re} - \sqrt{\frac{Ra}{Pr}} \omega T_0^n v_{z,im} + D(n_{ad} + 1) \frac{1}{T_0} P_{re} \\ &\quad - \sqrt{\frac{Ra}{Pr}} T_0^{n-1} T_{re} + \mu (k_x^2 + k_y^2) v_{z,re} \\ &\quad + \frac{1}{3} \mu k_x v'_{x,im} + \frac{1}{3} \mu k_y v'_{y,im} - \frac{4}{3} \mu' v'_{z,re} - \frac{2}{3} \mu' k_x v_{x,im} - \frac{2}{3} \mu' k_y v_{y,im}\end{aligned}\tag{E.11}$$

$$\partial_z T_{re} = T'_{re} \tag{E.12}$$

$$\begin{aligned}k_t \partial_z T'_{re} &= \sqrt{Pr Ra r} T_0^n T_{re} - \sqrt{Pr Ra \omega} T_0^n T_{im} - DP_{rr} P_{re} + DP_{r\omega} P_{im} \\ &\quad + k_t (k_x^2 + k_y^2) T_{re} - k_t' T'_{re} - \sqrt{Pr Ra} T_0^n v_{z,re}\end{aligned}\tag{E.13}$$

$$\begin{aligned}0 &= (\alpha n_{ad} + \beta) \epsilon D \sqrt{Pr r} \frac{1}{T_0^{n+1}} P_{re} - (\alpha n_{ad} + \beta) \epsilon D \sqrt{Pr \omega} \frac{1}{T_0^{n+1}} P_{im} \\ &\quad - \beta \epsilon \sqrt{Ra r} \frac{1}{T_0} T_{re} + \beta \epsilon \sqrt{Ra \omega} \frac{1}{T_0} T_{im} - n (D + \epsilon) \sqrt{Ra} \frac{1}{T_0} v_{z,re} \\ &\quad + \sqrt{Ra v} v'_{z,re} - \sqrt{Ra k_x} v_{x,im} - \sqrt{Ra k_y} v_{y,im}\end{aligned}\tag{E.14}$$

and the imaginary part (index im)

$$\partial_z v_{x,im} = v'_{x,im} \quad (\text{E.15})$$

$$\begin{aligned} \mu \partial_z v'_{x,im} = & \sqrt{\frac{Ra}{Pr}} r T_0^n v_{x,im} + \sqrt{\frac{Ra}{Pr}} \omega T_0^n v_{x,re} + k_x P_{re} + \mu \left(\frac{4}{3} k_x^2 + k_y^2 \right) v_{x,im} \\ & + \frac{1}{3} \mu k_x k_y v_{y,im} - \frac{1}{3} \mu k_x v'_{z,re} - \mu' v'_{x,im} - \mu' k_x v_{z,re} - \frac{1}{Ek} T_0^n v_{y,im} \end{aligned} \quad (\text{E.16})$$

$$\partial_z v_{y,im} = v'_{y,im} \quad (\text{E.17})$$

$$\begin{aligned} \mu \partial_z v'_{y,im} = & \sqrt{\frac{Ra}{Pr}} r T_0^n v_{y,im} + \sqrt{\frac{Ra}{Pr}} \omega T_0^n v_{y,re} + k_y P_{re} + \mu \left(k_x^2 + \frac{4}{3} k_y^2 \right) v_{y,im} \\ & + \frac{1}{3} \mu k_x k_y v_{x,im} - \frac{1}{3} \mu k_y v'_{z,re} - \mu' v'_{y,im} - \mu' k_y v_{z,re} + \frac{1}{Ek} T_0^n v_{x,im} \end{aligned} \quad (\text{E.18})$$

$$\partial_z v_{z,im} = v'_{z,im} \quad (\text{E.19})$$

$$\begin{aligned} \frac{4}{3} \mu \partial_z v'_{z,im} - \partial_z P_{im} = & \sqrt{\frac{Ra}{Pr}} r T_0^n v_{z,im} + \sqrt{\frac{Ra}{Pr}} \omega T_0^n v_{z,re} + D(n_{ad} + 1) \frac{1}{T_0} P_{im} \\ & - \sqrt{\frac{Ra}{Pr}} T_0^{n-1} T_{im} + \mu (k_x^2 + k_y^2) v_{z,im} \\ & - \frac{1}{3} \mu k_x v'_{x,re} - \frac{1}{3} \mu k_y v'_{y,re} - \frac{4}{3} \mu' v'_{z,im} + \frac{2}{3} \mu' k_x v_{x,re} + \frac{2}{3} \mu' k_y v_{y,re} \end{aligned} \quad (\text{E.20})$$

$$\partial_z T_{im} = T'_{im} \quad (\text{E.21})$$

$$\begin{aligned} k_t \partial_z T'_{im} = & \sqrt{PrRar} T_0^n T_{im} + \sqrt{PrRa\omega} T_0^n T_{re} - DP_{rr} P_{im} - DP_{r\omega} P_{re} \\ & + k_t (k_x^2 + k_y^2) T_{im} - k'_t T'_{im} - \sqrt{PrRa} T_0^n v_{z,im} \end{aligned} \quad (\text{E.22})$$

$$\begin{aligned} 0 = & (\alpha n_{ad} + \beta) \epsilon D \sqrt{Pr} r \frac{1}{T_0^{n+1}} P_{im} + (\alpha n_{ad} + \beta) \epsilon D \sqrt{Pr} \omega \frac{1}{T_0^{n+1}} P_{re} \\ & - \beta \epsilon \sqrt{Rar} \frac{1}{T_0} T_{im} - \beta \epsilon \sqrt{Ra\omega} \frac{1}{T_0} T_{re} - n(D + \epsilon) \sqrt{Ra} \frac{1}{T_0} v_{z,im} \\ & + \sqrt{Rav'}_{z,im} + \sqrt{Rak_x} v_{x,re} + \sqrt{Rak_y} v_{y,re}. \end{aligned} \quad (\text{E.23})$$

The equations for the eigenvalues

$$\partial_z \sqrt{Ra} = 0, \quad (\text{E.24})$$

$$\partial_z r = 0, \quad (\text{E.25})$$

$$\partial_z \omega = 0 \quad (\text{E.26})$$

guarantee their spacial uniformity.